



# Degradation of indometacin by simulated sunlight activated CDs-loaded BiPO<sub>4</sub> photocatalyst: Roles of oxidative species

Qianxin Zhang<sup>a</sup>, Ping Chen<sup>a</sup>, Meihui Zhuo<sup>a</sup>, Fengliang Wang<sup>a</sup>, Yuehan Su<sup>a</sup>, Tiansheng Chen<sup>a</sup>, Kun Yao<sup>a</sup>, Zongwei Cai<sup>b</sup>, Wenying Lv<sup>a</sup>, Guoguang Liu<sup>a,\*</sup>

<sup>a</sup> School of Environmental Science and Engineering, Institute of Environmental Health and Pollution Control, Guangdong University of Technology, Guangzhou, 510006, China

<sup>b</sup> Department of Chemistry, Hong Kong Baptist University, Hong Kong, China

## ARTICLE INFO

### Keywords:

Carbon dots

BiPO<sub>4</sub>

Reactive oxidative species

IDM

## ABSTRACT

In this study, novel carbon dots/BiPO<sub>4</sub> (CDBP) photocatalytic complexes were successfully synthesized via a facile hydrothermal-calcination synthesis strategy. The physicochemical properties of the synthesized samples were studied by X-ray diffraction (XRD), UV–vis diffuse reflectance spectra (DRS), Fourier infrared spectrometer (FT-IR), Raman spectrometer, scanning electron microscopy (SEM), high resolution transmission electron microscopy (HRTEM), photoluminescence spectra (PL), electrochemical workstation, etc. The activities of the CDBP were evaluated through the photocatalytic degradation of Indometacin (IDM) in an aqueous solution under simulated sunlight irradiation. With increasing concentrations of carbon dots (CDs), the photocatalytic activity of the CDBP initially increased, and then decreased. A CDs content of 3.0 wt% shows 12 times higher photocatalytic activity than that of pristine BiPO<sub>4</sub>. Reactive oxidative species, particularly O<sub>2</sub><sup>•−</sup> and h<sup>+</sup>, were the two critical reactive oxidative species to mediator immediate the photocatalytic degradation of IDM. A notable sign of 5, 5-dimethyl-1-pyrrolidone-N-oxyl (DMPOX) was observed through electron spin resonance spectroscopy (EPR) with CDBP as the photocatalyst, which indicated higher oxidability than pristine BiPO<sub>4</sub> under simulated sunlight irradiation. This enhanced photocatalytic activity might due to high-efficiency charge separation, unique up-converted PL properties, as well as the bandgap narrowing of the CDs. Moreover, the byproducts of IDM were detected by HPLC–MS/MS and GC–MS, and the probable pathways were deduced. The acute toxicity at three trophic levels initially increased slowly and then decreased rapidly as the IDM dechlorination and total organic carbon (TOC) decreased during photocatalytic degradation.

## 1. Introduction

Photocatalysts, particularly those with high stability and photocatalytic activity, have been regarded as hopeful materials for applications in energy and the treatment of pollutants [1,2]. To date, numerous photocatalysts, such as Bi-based photocatalysts, doped TiO<sub>2</sub> [3], Bi<sub>2</sub>O<sub>3</sub> [4], Bi<sub>2</sub>WO<sub>6</sub> [5], BiVO<sub>4</sub> [6] and BiOX [7] have been employed for the photocatalytic degradation of organics in wastewater or the ambient atmosphere. Since it was first reported by Pan, BiPO<sub>4</sub> has attracted remarkable interest due to its superior photocatalytic oxidation ability and stability [8]. However, BiPO<sub>4</sub> is only excited by ultraviolet light under 320 nm wavelengths (comprising < 4% of sunlight at the Earth's surface) due to its very wide band gap [9]. In order to extend the absorption band and reduce the band gap of BiPO<sub>4</sub> toward the improvement of its photocatalytic performance, BiPO<sub>4</sub> was composited

with BiOI [10], BiOBr [11], Ag<sub>3</sub>PO<sub>4</sub> [12], RGO [13], g-C<sub>3</sub>N<sub>4</sub> [14] and so on.

Carbon dots, as one of the carbonaceous materials, have attracted intense interest because of their many unique and novel properties, particularly, their high aqueous solubility, environmental compatibility, low toxicity, unique electron reservoir, photo-induced electron transfer property and outstanding up-converted photoluminescence (PL) behavior [15–19]. In addition, CDs with advantages of functional surface moieties, their extension of the visible light adsorption region and improved electron transfer [20–22]. Hence, carbon dots (CDs) might serve as promising components in the design of semiconductor composites. The design of complex photocatalysts (TiO<sub>2</sub>/CDs, g-C<sub>3</sub>N<sub>4</sub>/CDs) to enhance light utilization efficiency and photocatalytic performance has been achieved in our research group [23,24]. Considering the limitations of the BiPO<sub>4</sub> photocatalytic system and the remarkable

\* Corresponding author at: School of Environmental Science and Engineering, Guangdong University of Technology, No. 100 Waihan Xi Road, Guangzhou Higher Education Mega Center, Post Code: 510006, Guangzhou, China.

E-mail address: [liugg615@163.com](mailto:liugg615@163.com) (G. Liu).

<http://dx.doi.org/10.1016/j.apcatb.2017.09.008>

Received 15 June 2017; Received in revised form 29 July 2017; Accepted 4 September 2017

Available online 09 September 2017

0926-3373/ © 2017 Elsevier B.V. All rights reserved.

properties of CDs, the combination of CDs and  $\text{BiPO}_4$  may be regarded as a stable and efficient photocatalytic complex. To the best of our knowledge, few efforts have been made to combine CDs.

Recently, pharmaceutical and personal care products (PPCPs) have emerged as contaminants in ambient aquatic environments, which have attracted increasing concern, due to their potentially hazardous effects on ecosystems and humans [25–27]. Because of their stable chemical structures, and thus recalcitrance to biological degradation, they have been detected in urban wastewater cycles, and even in drinking water [28]. Some pharmaceuticals have been suspected of directly imparting toxicity to certain aquatic organisms [29]. Indometacin (IDM), a nonsteroid anti-inflammatory drug, was selected as a model compound for the study. IDM is used for the relief of mild to moderately severe pain accompanied by rheumatoid arthritis, inflammation, ankylosing spondylitis, and osteoarthritis. In sewage and surface water samples collected in the UK and Ireland IDM has been detected in the range of 5–792 ng/L [30]. Hence, a key issue is to urgently identify effective strategies for the degradation of water resident PPCPs.

In this study, monoclinic phase  $\text{BiPO}_4$  with high efficiencies and robust mineralization abilities, were synthesized via a simple hydrothermal method. The composite CDs/ $\text{BiPO}_4$  photocatalysts were prepared using a hydrothermal-calcination technique. The photocatalytic activity of CDs/ $\text{BiPO}_4$  on the degradation of Indometacin (IDM) was evaluated under simulated sunlight irradiation. In addition, the physicochemical properties and proposed enhancement mechanism of CDs/ $\text{BiPO}_4$  photocatalytic activity were also systematically investigated. During photocatalytic degradation, the probable degradation pathways, electron spin resonance (EPR), HPLC–MS/MS, GC–MS and the trapping experiment were measured to infer the kinetics of the system. An environmental risk assessment of the CDs/ $\text{BiPO}_4$  was investigated via the toxicity evolution characteristics of IDM.

## 2. Experimental

### 2.1. Materials

Indometacin (IDM, 98% purity) was obtained from TCI Reagent Co. Ltd. (China). Bismuth(III) nitrate pentahydrate ( $\text{Bi}(\text{NO}_3)_3 \cdot 5\text{H}_2\text{O}$ , 99% purity) and sodium phosphate tribasic dodecahydrate ( $\text{Na}_3\text{PO}_4 \cdot 12\text{H}_2\text{O}$ , 98% purity) were obtained from Aladdin (China). HPLC-grade methanol and acetonitrile were obtained from CNW Technologies GmbH (Germany). Analytical grade citric acid, urea, isopropanol, sodium azide,  $\text{Na}_2\text{C}_2\text{O}_4$ , acetic acid, and sulfuric acid were purchased from Taitan (China). Ultrapure water from a Milli-Q apparatus (Germany) was used throughout this study. All of the other chemical reagents were of analytical grade and used without further purification.

### 2.2. Preparation of photocatalysts

#### 2.2.1. Preparation of carbon dots (CDs) photocatalysts

The CDs were synthesized by a hydrothermal method [31]. In a typical experiment, 3.0 g citric acid and 1.0 g urea were combined in a beaker under magnetic stirring and dissolved in 10 mL of DI water. The solution was transferred to a 100 mL Teflon-lined stainless steel autoclave and maintained at 180 °C for 5 h. After cooling to room temperature, the large particles were removed by centrifugation at 10000 rpm for 30 min. Subsequently, the CDs solution was dried overnight at 70 °C to obtain CDs powder.

#### 2.2.2. Preparation of $\text{BiPO}_4$ photocatalysts

The  $\text{BiPO}_4$  was synthesized via a hydrothermal process [32]. In a typical experiment, 3 mmol of  $\text{Bi}(\text{NO}_3)_3 \cdot 5\text{H}_2\text{O}$  and 30 mL distilled water were combined in a beaker under magnetic stirring. An equal molar of  $\text{Na}_3\text{PO}_4 \cdot 12\text{H}_2\text{O}$  was then added into the mixture and stirred for 2 h at room temperature. The solution was subsequently transferred to a 100 mL Teflon-lined stainless steel autoclave and maintained at 180 °C

for 48 h. Subsequently, the products were rinsed several times with distilled water, or absolute alcohol, and dried at 80 °C for 12 h.

#### 2.2.3. Preparation of CDs/ $\text{BiPO}_4$ photocatalysts

The CDs/ $\text{BiPO}_4$  (CDBP) was synthesized via a facile hydrothermal-calcination method. Different amounts of CDs and  $\text{BiPO}_4$  were accurately weighed and put into a beaker. The mixed powder was ultrasonically dispersed in 20 mL of ethanol, subsequently transferred to an alumina crucible, and stirred to dry in a fuming cupboard. The alumina crucible containing the dry-powder was then transferred to a muffle furnace at 300 °C for 3 h. After cooling to room temperature, the light-gray powder was collected through filtration. Similarly, 1.0 wt%, 3.0 wt%, 5.0 wt%, and 7.0 wt% of the CDBP was prepared by the same route.

### 2.3. Characterization

The crystallinity of the CDBP samples were characterized by X-ray diffraction (XRD) with a Rigaku Ultima III diffractometer (CuK $\alpha$ , voltage 35 kV, electrical current 20 mA) using Cu K $\alpha$  radiation ( $\lambda = 0.15418$  nm) at a scanning rate of 8°/min. in the  $2\theta$  range of 10–60°. Field emission scanning electron microscopy (SEM) images of the CDBP were obtained with a JSM-7001F (Japan) system. The crystal planes and fringes of the samples were obtained by a high-resolution transmission electron microscope (HRTEM, JEM-2100F). A PHI Quantera 2X was employed for X-ray photoelectron spectroscopy (XPS) testing with non-monochromated Mg-K $\alpha$  radiation as the excitation source. Brunauer-Emmett-Teller (BET) surface area and porosity measurements were carried out by  $\text{N}_2$  adsorption at –196 °C using a Autosorb-IQ (USA) instrument. The UV–vis diffuse reflectance spectra (DRS) were tested on a Shimadzu UV-2550 UV–vis spectrophotometer at room temperature. A Thermofisher Nicolet 6700 spectrometer (Thermofisher, USA) was employed to record FT-IR spectra in the range of from 4000 to 400  $\text{cm}^{-1}$ . Photoluminescence (PL) spectra were measured with a FLS980 Series of Fluorescence Spectrometers (UK). The photocurrents and electrochemical impedance spectroscopy of CDBP were performed with an Autolab PGSTAT302N electrochemical system (Metrohm) using a standard three-electrode cell under simulated sunlight irradiation. The intensity of light at the film electrode was 1.5 mW/cm $^2$ , and 0.1 mol/L of  $\text{Na}_2\text{SO}_4$  was used as the electrolyte. The photoelectric responses of the sample under light-on and light-off conditions were measured at 0.0 V.

### 2.4. Photocatalytic activity tests

#### 2.4.1. Photocatalytic experiments and analytical method

The photocatalytic performance of the CDBP was evaluated via the photocatalytic degradation of IDM under simulated sunlight irradiation. The photocatalytic experiment was carried out in a XPA-7 rotary photocatalytic reactor (Nanjing Xujiang), as shown in Fig. S1 (inset). The simulated sunlight source was provided by a 350 W xenon lamp with a 290 nm cut-off filter (Fig. S1). For each experiment, 4 mg/L IDM and 1.0 g/L catalysts were added into a 50 mL quartz tube. Prior to light irradiation, the adsorption equilibrium for IDM on the photocatalyst was provided by ultrasound for 1 h and stirring in the dark for 30 min. Following a certain time interval, 2.0 mL samples were filtered in order to remove the particles with a 0.22  $\mu\text{m}$  Millipore filter. The photocatalytic experiments were conducted in triplicate, and the results were averaged in the analysis. The concentration of IDM was analyzed by high performance liquid chromatography (HPLC). The total organic carbon (TOC) was measured via a TOC analyzer (Shimadzu, TOC-V CPH E200 V, Japan). Both HPLC/MS/MS (Agilent Technologies, USA) and GC/MS (Agilent 6890-GC/5973i-MS) were adopted to identify degradation products, with the details of the analytical methods conveyed in the SI.

#### 2.4.2. Determination of ROSs

ROSs scavenging experiments were conducted in order to determine the reactive oxidative species (ROSs) that were generated during the IDM photodegradation procedure. Sodium oxalate ( $\text{Na}_2\text{C}_2\text{O}_4$ ) as hole ( $h^+$ ) scavengers, Isopropanol (IPA) as hydroxyl radical ( $\cdot\text{OH}$ ) scavengers,  $\text{NaN}_3$  as hydroxyl radical ( $\cdot\text{OH}$ ) and singlet oxygen ( $^1\text{O}_2$ ) scavengers, and 4-hydroxy-2,2,6,6-tetramethylpiperidinyloxy (TMPOL) as superoxide ( $\text{O}_2^{\cdot-}$ ) radical scavengers were employed [23,33].

In order to directly detect the ROSs, electron paramagnetic resonance (EPR, Bruker E500 spectrometer, Germany) was used. Following simulated sunlight irradiation with 0.05 g/L catalyst and 50 mM DMPO in water for  $\cdot\text{OH}$ , or in methanol, for  $\text{O}_2^{\cdot-}$ , the DMPO- $\text{OH}$  or DMPO- $\text{O}_2^{\cdot-}$  EPR signals were measured at different time intervals. The following ESR conditions for the detection of  $\cdot\text{OH}$  were established: microwave frequency of 9056.652 MHz, power of 0.998 mW, phase of 531, coupling of 209, sweep width of 5 mT, sweep time of 1 min, and center field of 323.162 mT.

#### 2.5. Ecotoxicity assessment

Three trophic levels of acute toxicity experiments, luminescent bacteria *V. fischeri* (15 min), *D. magna* (48 h), and *Chlorella* (96 h) were employed to assess the environmental risks of CDBP as a photocatalyst during the degradation of IDM. An initial concentration of 4 mg/L IDM and its byproducts during photocatalytic degradation was used to estimate acute toxicity. According to the Water Quality Determination of the Acute Toxicity-Luminescent Bacteria Test (GB/T15441-1995) *V. fischeri* was employed to measure the change of toxicity with a Microtox Model DXY-2 Toxicity Analyzer. According to the Chemicals-Alga Growth Inhibition Test (GB/T21805-2008), the *Chlorella vulgaris* bioassay was assessed by monitoring algae growth in vitro with a UV-vis spectrophotometer (UV759S, Shanghai) following different exposure times. The *D. magna* followed the guidance of the OECD (1981) [34]. Mobilization was evaluated after 24 and 48 h of exposure, with experimental medium containing 220 mg/L  $\text{CaCl}_2$ , 65 mg/L  $\text{NaHCO}_3$ , 60 mg/L  $\text{MgSO}_4$ , and 6 mg/L KCl. Each assay was performed in triplicate.

### 3. Results and discussions

#### 3.1. Characterization

Fig. 1a shown the TEM, HRTEM and size distribution of CDs. The TEM image in Fig. 1a reveals the spherical morphology of CDs. The average diameter of CDs was ca. 5.5 nm (inset of Fig. 1a). HRTEM image (inset of Fig. 1a) clearly displays the crystalline structure of the CDs, with lattice spacing of 0.32 nm, corresponding well to the (002) lattice planes of graphite, which indicated that the CDs possessed a crystalline graphitic carbon structure [35].

The fluorescence tests revealed the superior up-converted photoluminescence properties of the CDs (Fig. 1b). The up-converted emissions were remarkably located in the range of from 350 nm to 700 nm, when excited by long-wavelength light, from 400 nm to 900 nm. The insert indicates that CDs demonstrated a bright blue emission by 365 nm UV lamp irradiation. As is depicted in Fig. 1c, the UV-vis absorption of the CDs in an aqueous solution exhibited broader UV-vis absorption, in the range of from 300 nm to 400 nm. The CDs also showed two characteristic peaks centered at 235 nm and 330 nm, which might be attributed to the  $n\text{-}\pi^*$  transitions of the  $\text{C}=\text{O}$  bands and the  $\pi\text{-}\pi^*$  transition of aromatic  $\text{sp}^2$  conjugate domains [20,36,37]. These results suggested as-prepared CDs might enhance photocatalytic efficiency through the enhanced transfer of electronic capabilities and augmented light absorption.

The UV-vis DRS spectra of pure  $\text{BiPO}_4$  and CDBP were measured to evaluate their light absorption properties. As shown in Fig. 1d, the pure  $\text{BiPO}_4$  exhibited the typical absorption edge at  $\sim 323$  nm, which is

consistent with reported values [8]. However, the absorbance of CDBP nanocomposites was enhanced at the range of from 300 to 450 nm in comparison with that of  $\text{BiPO}_4$  due to the existence of the CDs, which suggested that CDBP photocatalysts may more efficiently absorb the solar spectra. It is widely known that a wavelength red-shift always means that the band gap of the photocatalyst is narrowing. As illustrated in the inset of Fig. 1d, the  $\text{BiPO}_4$  and CDBP presented band gaps of 3.84 eV and 3.52 eV, respectively. An enhanced light harvesting ability and decreased band gap were both beneficial toward enhancing the photocatalytic activity of  $\text{BiPO}_4$ .

Fig. 1e depicts the XRD patterns of the as-synthesized CDBP composites and pure  $\text{BiPO}_4$ . It can be seen that all of the diffraction peaks in the XRD pattern of CDBP could be indexed into the monoclinic phase of pure  $\text{BiPO}_4$  (space group P21/n, JCPDS 80-0209) with cell parameters of  $a = 6.763$  Å,  $b = 6.952$  Å, and  $c = 6.482$  Å. The diffraction peak at  $2\theta = 25.3^\circ$ ,  $27.1^\circ$ ,  $29.1^\circ$ , and  $31.2^\circ$  may be indexed to (111), (200), (120), and (012) crystal planes of monoclinic  $\text{BiPO}_4$  which revealed that the CDs doping did not significantly alter the crystal structure of  $\text{BiPO}_4$ . The diffraction peaks of CDs at  $26^\circ$  was too weak to be observed, which was due to the relatively small quantity of CDs in the composites [38]. However, as illustrated in the inset of Fig. 1e, a careful comparison of the diffraction peaks in the range of from  $25 - 30^\circ$  showed that the peak position of  $\text{BiPO}_4$  shifted slightly toward a higher  $2\theta$  value, which was also the case for fluorine doped  $\text{BiPO}_4$  [39]. According to Bragg's law (Eq. (1)),  $2d_{hkl}\sin\theta = n\lambda$  (1), where  $\lambda$  is the X-ray wavelength,  $\theta$  is the diffraction angle of the crystal plane ( $hkl$ ) and  $d_{hkl}$  is the distance between crystal planes of ( $hkl$ ). The observed shift of the diffraction peak toward a higher angle could result in the decrease of the  $d_{hkl}$  value, which might be due to the extrusion of the carbon dots. The diffraction pattern of the CDBP composites was uncontaminated, suggesting that the product was relatively pure.

Fig. 2 To directly confirm the morphologies of  $\text{BiPO}_4$  and CDBP, they were characterized by SEM and HRTEM. As can be seen from the SEM images, the pure  $\text{BiPO}_4$  had a nanorod shape (Fig. 2a) [32]. The morphology of the CDBP composite photocatalyst was practically the same as that of the  $\text{BiPO}_4$  nanorod (Fig. 2b). The structure of CDBP was further exhibited by the EDS mapping and HRTEM images (Fig. 2c-j). Bi, P, O, C elements were all existed in 3.0 wt% CDBP composite photocatalyst. C element distributed the main body of CDs and were enriched on the surface of  $\text{BiPO}_4$  nanorod. As confirmed in the HRTEM of CDBP (Fig. 2i), the CDs were loaded onto the surfaces of the photocatalysts. The lattice fringes of 0.467 nm and 0.32 nm belonged to the lattice plane of  $\text{BiPO}_4$  (JCPDS 80-0209) (011) and CDs (002), respectively [35].

Fig. 3 Raman spectra were recorded to further verify the presence of the CDs within the complex structures of the CDBP. Two typical characteristic peaks located at approximately  $1361\text{ cm}^{-1}$  (D-band) and  $1603\text{ cm}^{-1}$  (G-band), corresponded to the D-band and G-band of carbon, respectively, which can be observed in the inset of Fig. 3a. The D-band centered at  $1361\text{ cm}^{-1}$  was attributed to the extent of the defects of  $\text{sp}^3$  carbon atoms, whereas the G-band at  $1603\text{ cm}^{-1}$  was put down to the  $\text{sp}^2$  carbon atoms, which would enhance [40]. Fig. 3b shows the FT-IR spectra of CDs,  $\text{BiPO}_4$  and the related photocatalyst complex. For the FT-IR spectra of CDBP, the vibrational peaks of  $\text{PO}_4^{3-}$  ions were observed at  $414\text{--}1083\text{ cm}^{-1}$  [41]. After the introduction of CDs, the characteristic peaks of  $\text{C}=\text{C}-\text{H}$ ,  $\text{CH}_2$ , and  $\text{C}=\text{O}$  were observed at  $3133$ ,  $2969\text{ cm}^{-1}$  and  $1630\text{ cm}^{-1}$ , testified to the existence of CDs in the photocatalyst complex [23,38]. On the side, no significant change of  $\text{BiPO}_4$  could be seen, which was due to its stable crystal phase.

The  $\text{N}_2$  adsorption-desorption isotherms for  $\text{BiPO}_4$  and CDBP systems were shown on Fig. S2. As it can be noticed,  $\text{BiPO}_4$  and CDBP show similar surface features. A type IV isotherm with clear H1 type adsorption hysteresis loop has been obtained in both  $\text{BiPO}_4$  and CDBP, indicating their narrow distribution mesoporous structure. The CDBP composites show an isotherm resulting from the mixture of pristine  $\text{BiPO}_4$ . Moreover, the obtained specific surface area for the  $\text{BiPO}_4$  and



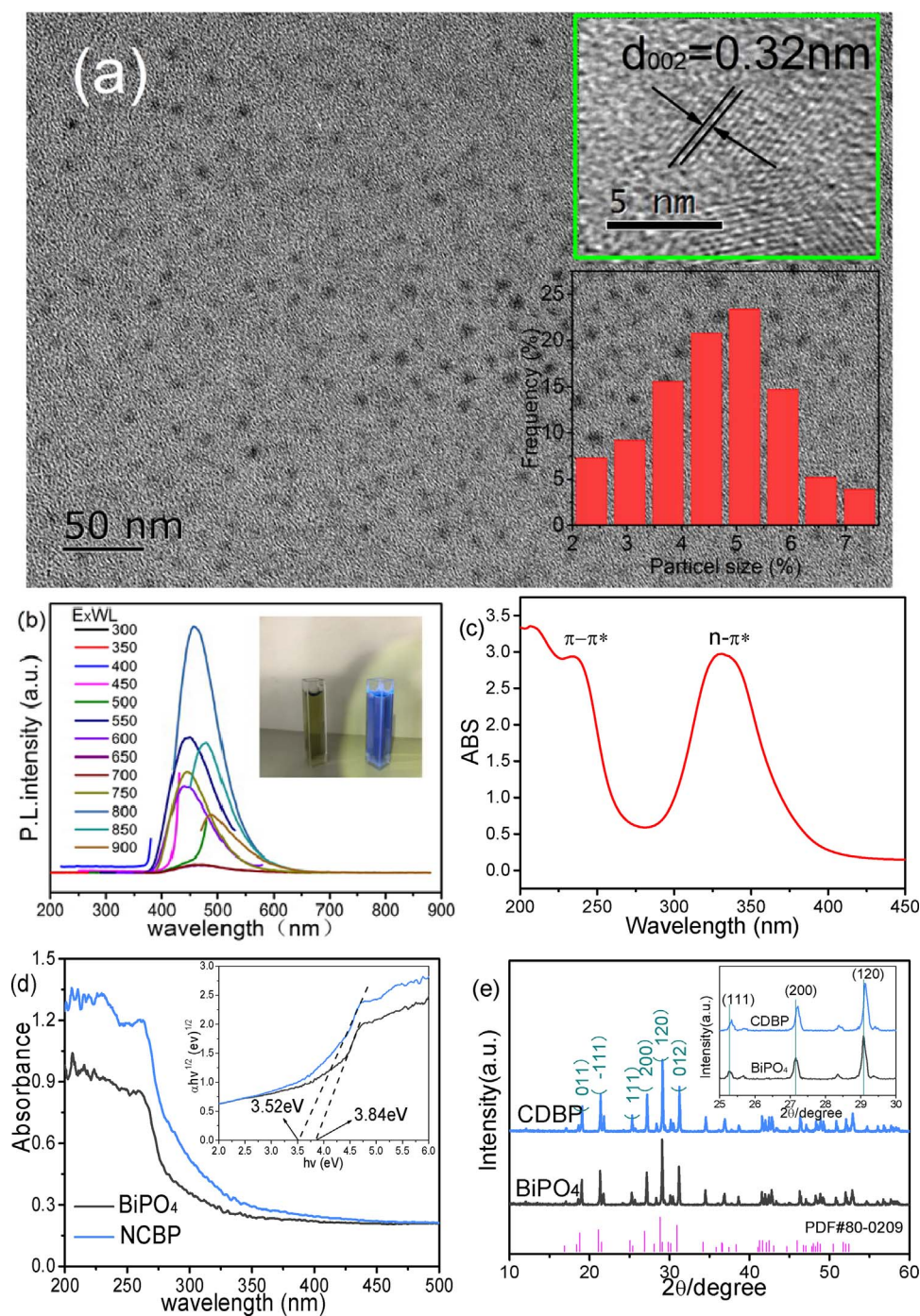


Fig. 1. (a) The TEM, HRTEM and size distribution of CDs; (b) Up-converted photoluminescence spectra of CDs, inset: C-Dots dispersed in water illuminated under UV light; (c) UV-vis absorption spectra of the CDs; (d) UV-vis diffuse reflectance absorbance spectra of  $\text{BiPO}_4$  and 3.0wt%CDBP, inset: The band gap of  $\text{BiPO}_4$  and 3.0wt%CDBP determined from the  $(ah\nu)^{1/2}$  versus photon-energy; (e) XRD spectrum of  $\text{BiPO}_4$  and 3.0wt%CDBP, inset: high-definition spectrum  $2\theta = 25^\circ\text{--}30^\circ$ .

CDBP were 2.604 and 1.475  $\text{m}^2/\text{g}$ , which might be due to the  $\text{BiPO}_4$  were blocked by CDs.

Fig. 4 shows the X-ray photoelectron spectroscopy (XPS) data for CDBP compared to that of pristine  $\text{BiPO}_4$ . The survey spectra of CDBP samples revealed the predominant presence of phosphate (P2p, 132.6 eV), bismuth (Bi4f, 159.6 eV), carbon (C1s, 284.6 eV), and oxygen (O1s, 530.6 eV) (Fig. 4a). In addition, C1s was split into two peaks at 284.77 and 286.47 eV, which could be assigned to C–C, and C–N, respectively [42,43]. Moreover, it is also noted that when comparing pristine  $\text{BiPO}_4$  with CDBP, the binding energy of Bi4f and P2p exhibited a positive shift (Fig. 4b), which was also recorded in the  $\text{C}_3\text{N}_4/\text{BiPO}_4$  complex [44]. These results revealed that the interaction between  $\text{BiPO}_4$  and CDs was not simple physical adsorption, which concurred with the results of the FT-IR and Raman.

From the above, the CDs were successfully loaded onto the surface of the  $\text{BiPO}_4$ , which could enhance the photocatalytic abilities of  $\text{BiPO}_4$  by transforming its electron dynamics, and broadening the capacity for the absorption of light.

### 3.2. Photocatalytic performance: photodegradation of Indometacin (IDM)

Fig. 5 To evaluate the simulated sunlight ( $\lambda \geq 290$  nm) activity of the prepared  $\text{BiPO}_4$  and CDBP photocatalyst complexes, this paper examined the photocatalytic degradation of a typical personal care product (PPCP), Indometacin (IDM). As Fig. 5a shows, following the adsorption/desorption equilibrium of IDM on the surface of the  $\text{BiPO}_4$  and the related photocatalyst complexes, the adsorbent dosage of IDM was less than 3.0%. Thus, the photocatalyst adsorption of IDM was not the

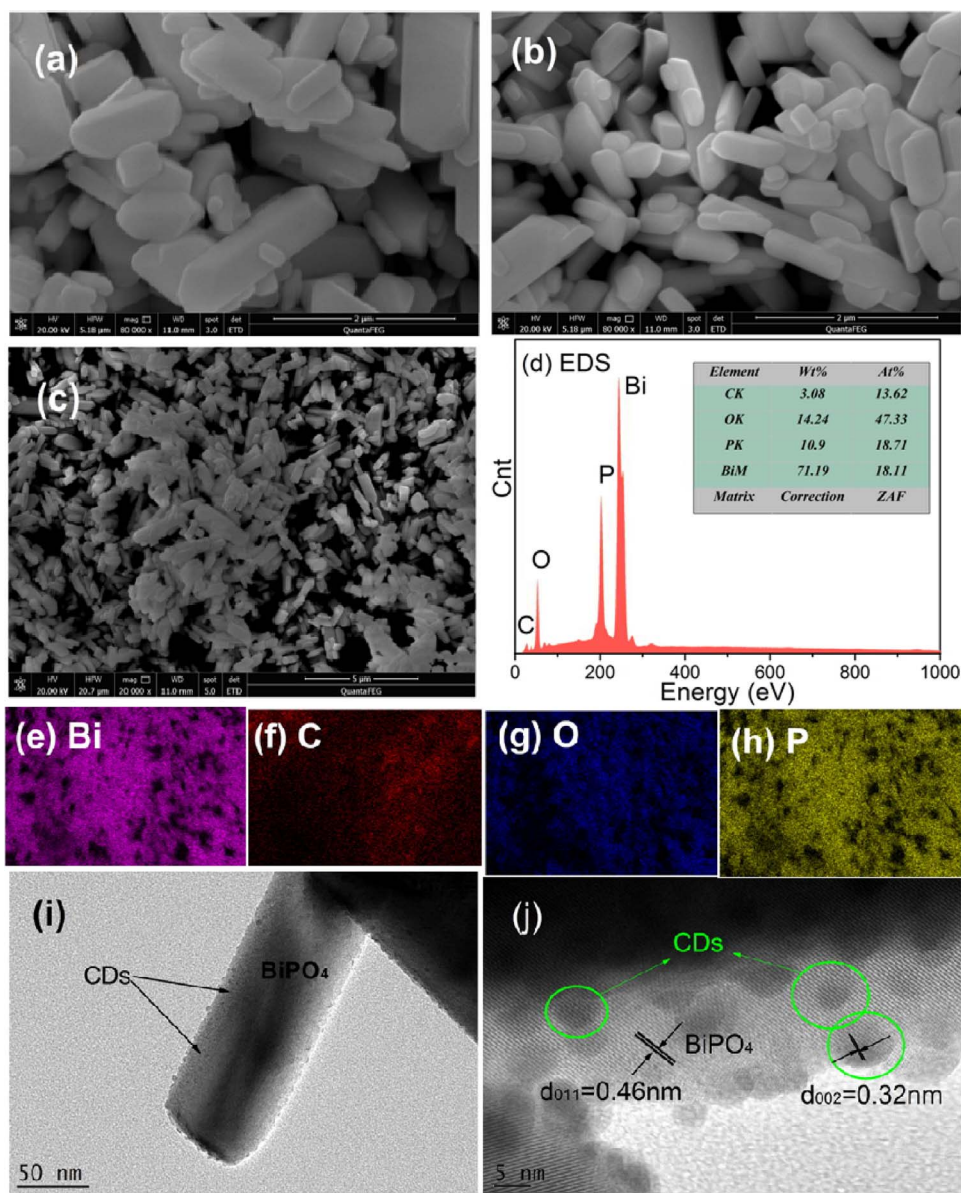


Fig. 2. SEM image of pristine BiPO<sub>4</sub> (a) and CDBP composites(b);(c-h)EDSmapping of CDBP; (i-j)TEM image of CDBP.

primary focus of study. Compared to photolysis ( $0.0007 \text{ min}^{-1}$ ) without catalysts, the introduction of BiPO<sub>4</sub> increased the degradation rate constant to  $0.0015 \text{ min}^{-1}$  (Fig. 5b). However, only 16% of the IDM was degraded by pure BiPO<sub>4</sub> following 120 min of simulated sunlight irradiation. With the presence of CDs, the IDM degradation was

obviously faster than for the pure BiPO<sub>4</sub>. This was because the up-converted CDs enhanced the photocatalytic abilities of BiPO<sub>4</sub>, to effectively degrade IDM. The 3.0wt%CDBP composites appeared to be optimal for the photocatalytic degradation of IDM. As Fig. 5b shows, it was clearly demonstrated that the photocatalytic activity of 3 wt%

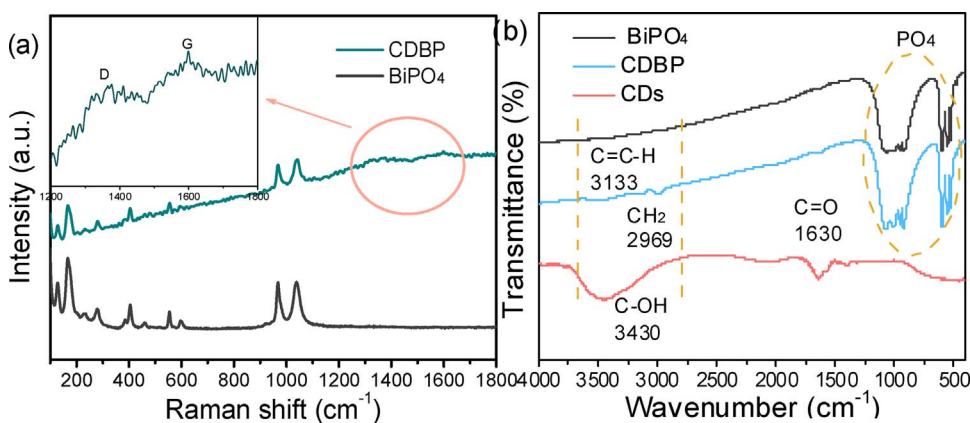


Fig. 3. (a) Raman spectrum of BiPO<sub>4</sub> and CDBP composites, inset: high-definition spectrum from  $1200 \text{ cm}^{-1}$  to  $1800 \text{ cm}^{-1}$ ; (b) FT-IR spectra of BiPO<sub>4</sub> and 3.0 wt% CDBP composites and CDs.



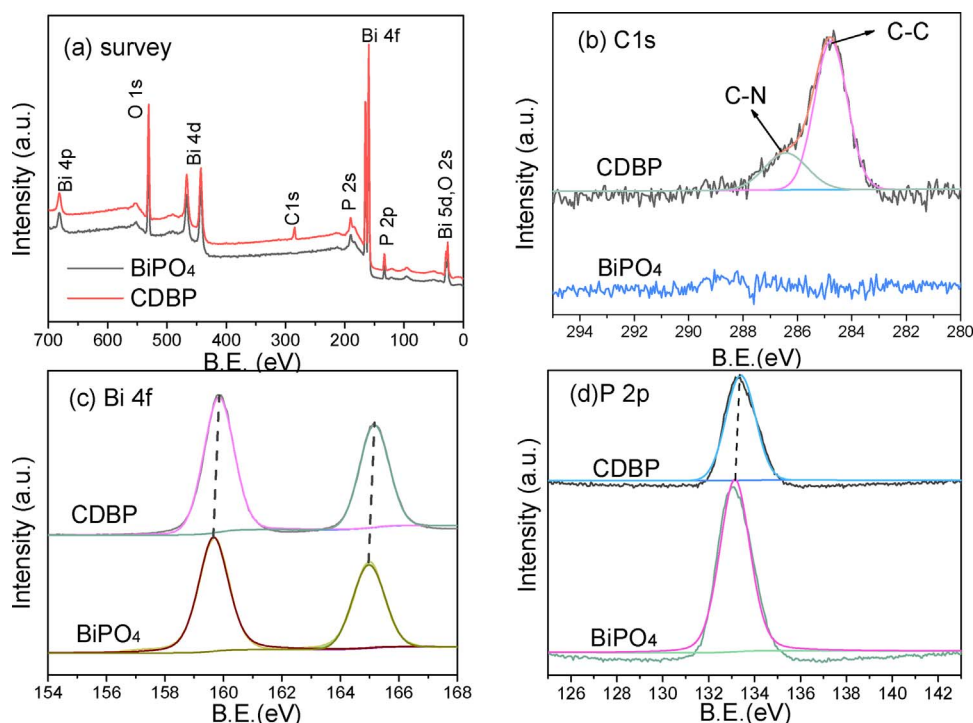


Fig. 4. XPS analysis of  $\text{BiPO}_4$  and 3.0 wt% CDBP composites: (a) the full-scale XPS spectrum; High resolution XPS spectra of C1s(b), Bi4f (c), and P2p (d).

CDBP was 12, 5, 2, and 1.7 times higher than that of pristine  $\text{BiPO}_4$ , 1 wt% CDBP, 5 wt% CDBP, and 7.0 wt% CDBP, respectively, under simulated sunlight irradiation. These results indicated that CDBP played a critical role in enhancing the photocatalytic activity of  $\text{BiPO}_4$ , and revealed a synergistic catalytic effect of the CDBP composite. Meanwhile, it was shown that the appropriate concentration of CDs markedly enhanced the photocatalytic abilities of  $\text{BiPO}_4$ ; however, an excess CDs ( $> 3.0$  wt%) resulted in decreased degradation rates, which is discussed in the following section.

As mentioned above (Fig. 1b, and c), pure  $\text{BiPO}_4$  exhibited absorption in the region of 325 nm, while the absorption intensity was

broadened with the introduction of CDs. This might be regarded as one of the key reasons for the enhancement of photocatalytic activity under simulated sunlight illumination. However, excess CDs ( $> 3.0$  wt%) led to an obvious decrease of photocatalytic activity (Fig. 5a). Higher CDs content within the composites might lead to an inner filter effect, via competition with  $\text{BiPO}_4$  for the absorption of photons [45]. Furthermore, excess CDs might impede the surface adsorption of IDM and reactive species on the composite photocatalyst. In short, it was obvious that the introduction of CDs to  $\text{BiPO}_4$  could enhance the simulated sunlight photocatalytic activity of the composites.

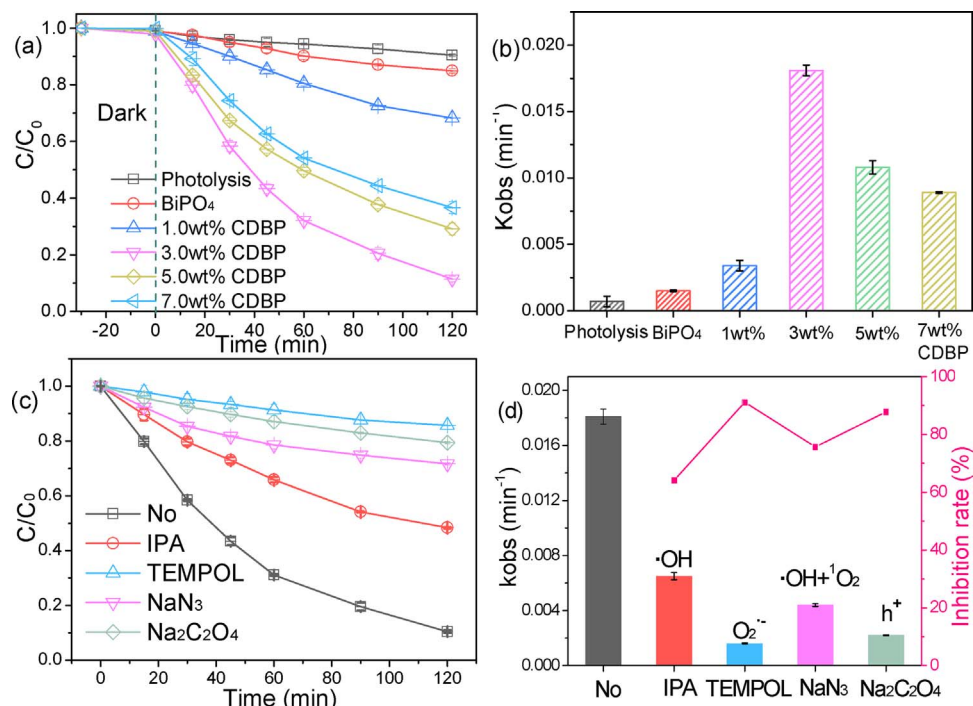


Fig. 5. (a) Photocatalytic degradation of IDM with different photocatalysts under simulated sunlight irradiation; (b) Kinetic rate constant of IDM degradation over different photocatalysts; (c) Photocatalytic degradation of IDM under simulated sunlight irradiation with addition of different scavengers using 3.0 wt% CDBP photocatalyst. (d) Kinetic rate constant of IDM (bar, left y-axis) and the inhibition rate of ROS (pink curve, right y-axis).

### 3.3. Roles of oxidative species

Generally, during the process of the photocatalytic degradation of IDM, various reactive oxidative species (ROS) may be generated, which play different roles. Therefore, in order to further identify their role in the degradation of IDM in this system, different scavengers were employed in this study. Typically, sodium oxalate ( $\text{Na}_2\text{C}_2\text{O}_4$ ) as hole ( $\text{h}^+$ ) scavengers, Isopropanol (IPA) as hydroxyl radical ( $\cdot\text{OH}$ ) scavengers,  $\text{NaN}_3$  as hydroxyl radical ( $\cdot\text{OH}$ ) and singlet oxygen ( $^1\text{O}_2$ ) scavengers, and 4-hydroxy-2,2,6,6-tetramethylpiperidinyloxy (TEMPL) as superoxide ( $\text{O}_2^{\cdot-}$ ) radical scavengers were used [23,33]. As Fig. 5c and d reveal, without the addition of scavengers a more rapid degradation of IDM was observed, with a photocatalytic degradation rate constant of  $0.0181 \text{ min}^{-1}$ . However, the addition of IPA and  $\text{NaN}_3$  inhibited the degradation of IDM, with rate constants of only  $0.0065 \text{ min}^{-1}$  and  $0.0044 \text{ min}^{-1}$ . These results indicated that  $^1\text{O}_2$  showed a negligible effect, with inhibition rates of 11.6%, which was similar to Wang et al. [24]. Instead, with the addition of IPA as an  $\cdot\text{OH}$  scavenger, an inhibited degradation of IDM was observed, with inhibition rates of 64.1%. Notably, with the addition of  $\text{Na}_2\text{C}_2\text{O}_4$ , the rate constant decreased to  $0.0022 \text{ min}^{-1}$ , which suggested that 87.8% of the rate originated from  $\text{h}^+$ . This result indicated that  $\text{h}^+$  played a significant role in photocatalytic degradation of IDM, likely through a direct electron transfer process. The rate constant was reduced to  $0.0016 \text{ min}^{-1}$  in the presence of TEMPL, suggesting that 91.2% of the rate originated from  $\text{O}_2^{\cdot-}$ . These results demonstrated the important roles of  $\cdot\text{OH}$  and  $\text{O}_2^{\cdot-}$  in the degradation of IDM [24].

To investigate the photocatalytic mechanism in detail, we conducted spin-trapping ESR of  $\text{BiPO}_4$  and CDBP in an aqueous dispersion of  $\text{DMPO} \cdot \cdot\text{OH}$  and in a methanol dispersion of  $\text{DMPO} \cdot \text{O}_2^{\cdot-}$ . As shown in Fig. 6a, no ESR signals could be found when the system remained in the dark. No EPR signals were observed for  $\text{BiPO}_4$  under simulated sunlight irradiation, as is shown in Fig. 6a, indicating the absence of  $\cdot\text{OH}$  on the as-prepared  $\text{BiPO}_4$ , which was likely due to the low-concentration of  $\cdot\text{OH}$ . However, the hyperfine splitting of 5,5-dimethyl-2-oxo-pyrroline-1-oxyl (DMPO-X) was distinctly observed on CDBP under simulated sunlight irradiation [46]. The emergence of DMPO might due to the photogenerated holes that directly oxidized DMPO, which indicated the highly-efficient oxidation properties of CDBP under the simulated sunlight [47]. In addition, this might be the main reason that CDBP possesses high simulated sunlight photocatalytic activity following NCD hybridization. The fact that we did not yet detect  $\cdot\text{OH}$  radicals via the EPR test, does not mean that they were absent.

As shown in Fig. 6b, four-line ESR signals with intensity ratios of 1:1:1:1 were observed for both  $\text{BiPO}_4$  and CDBP under simulated sunlight irradiation, which represented the presence of  $\text{DMPO} \cdot \text{O}_2^{\cdot-}$  adducts [48]. Notably, however, higher  $\text{O}_2^{\cdot-}$  formation rates were also observed with the CDBP system in contrast to  $\text{BiPO}_4$ , which indicated that the CDBP was more amenable in the formation of superoxide radicals. According to the results shown in Fig. 6b, the IDM degradation

rate was higher in the presence of CDBP composites than pure  $\text{BiPO}_4$ . This implied that the CDBP composite increased the generation of  $\text{O}_2^{\cdot-}$ , where the oxidizing ability led to a higher IDM degradation rate.

### 3.4. Byproducts and ROS-induced pathways

HPLC/MS/MS and GC/MS were utilized to identify the byproducts formed during the photocatalytic degradation of IDM. The byproduct information is also summarized in Table S1, Fig. S5, Table S2 and Fig. S6. As shown in Table S1, nine products were identified by HPLC/MS/MS, and three were identified by GC/MS (Table S2). According to our preliminary work [24], the C3, C4, and C7 sites of IDM (Fig. S3), with higher  $\text{FED}_{\text{HOMO}}^2 + \text{FED}_{\text{LUMO}}^2$  values, were more likely to be attacked by  $\cdot\text{OH}$  via an electrophilic reaction, while the C1, C7, C12, C17, and C19 sites, having lower  $\text{FED}_{\text{HOMO}}^2 + \text{FED}_{\text{LUMO}}^2$  values, may likely be attacked by  $\text{O}_2^{\cdot-}$  via nucleophilic addition reactions [49]. As seen in Scheme 1, three major pathways might be involved in the photocatalytic degradation of IDM.

Pathway I:  $\text{O}_2^{\cdot-}$  involved the attack C7 by a nucleophilic reaction, leading to the formation of a peroxide, and subsequently, C–N bond cleavage and the formation of P1 and P4. The same byproducts were reported by Nováková et al. [50] and Wang et al. [24]. Because of the  $\text{e}^-$  reductive mechanism, the P4 were attacked on C1–Cl by dechlorination [51]. Benzoic acid radicals were formed, which were oxidized by  $\cdot\text{OH}$  to generate P12. Moreover, P11 were formed by the decarboxylation reaction of P1, and were further oxidized by  $\cdot\text{OH}$  to generate P10.

Pathway II: The formation of the C11 methyl radical was thought to proceed via the mesolytic cleavage, when ROS attacks the C12 [52]. The IDM frontier electron density calculations also indicated that C12 was the most likely site for  $\text{O}_2^{\cdot-}$  attack. Following decarboxylation, the C11 methyl radical underwent a hydrogen shift leading to P9, which could be attacked by  $\text{O}_2^{\cdot-}$  leading to the cleavage of the C8–C10 double bond and the formation of a peroxide to generate P8. Otherwise, P9 could also be further oxidized by ROS to generate P3, which was identified by Fabio et al. [53]. Further, the C10-central radical was formed through decarbonylation, and subsequently, P2 was formed via the addition of  $\cdot\text{OH}$ .

Pathway III: The C3 was  $\cdot\text{OH}$ -substituted due to higher  $\text{FED}_{\text{HOMO}}^2 + \text{FED}_{\text{LUMO}}^2$  values. Meanwhile, the P5 intermediate resulted from the  $\cdot\text{OH}$ -addition of the C8, C10 double bond. Subsequently, the P6 intermediate was formed by the dehydration of P5 before the  $\cdot\text{OH}$ -substituted C3. The P6 intermediate was further oxidized by ROS to generate P7, which might attack the amide bond by  $\cdot\text{OH}$  via an electrophilic reaction to give P2 and P11.

Further, under prolonged irradiation time, the IDM and its byproducts could be completely mineralized to  $\text{CO}_2$  and  $\text{H}_2\text{O}$ . In summary, the results of HPLC/MS/MS and GC/MS analyses, as well as the proposed pathways illustrate the important roles of  $\cdot\text{OH}$  and  $\text{O}_2^{\cdot-}$  over the reaction with IDM. This finding is in accordance with above results of

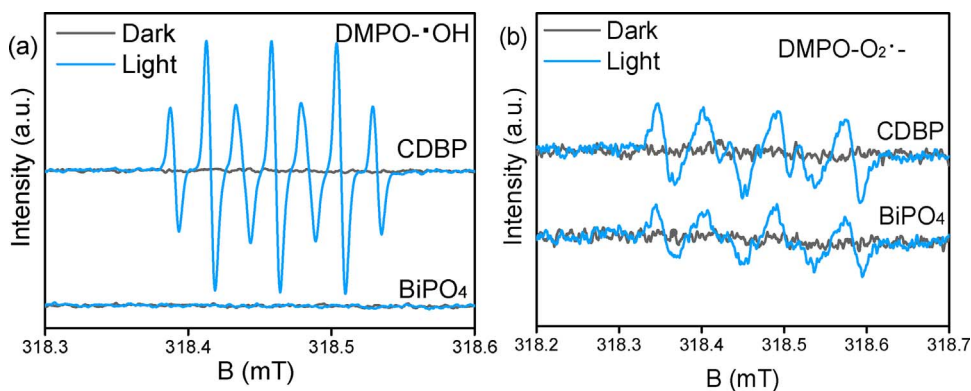
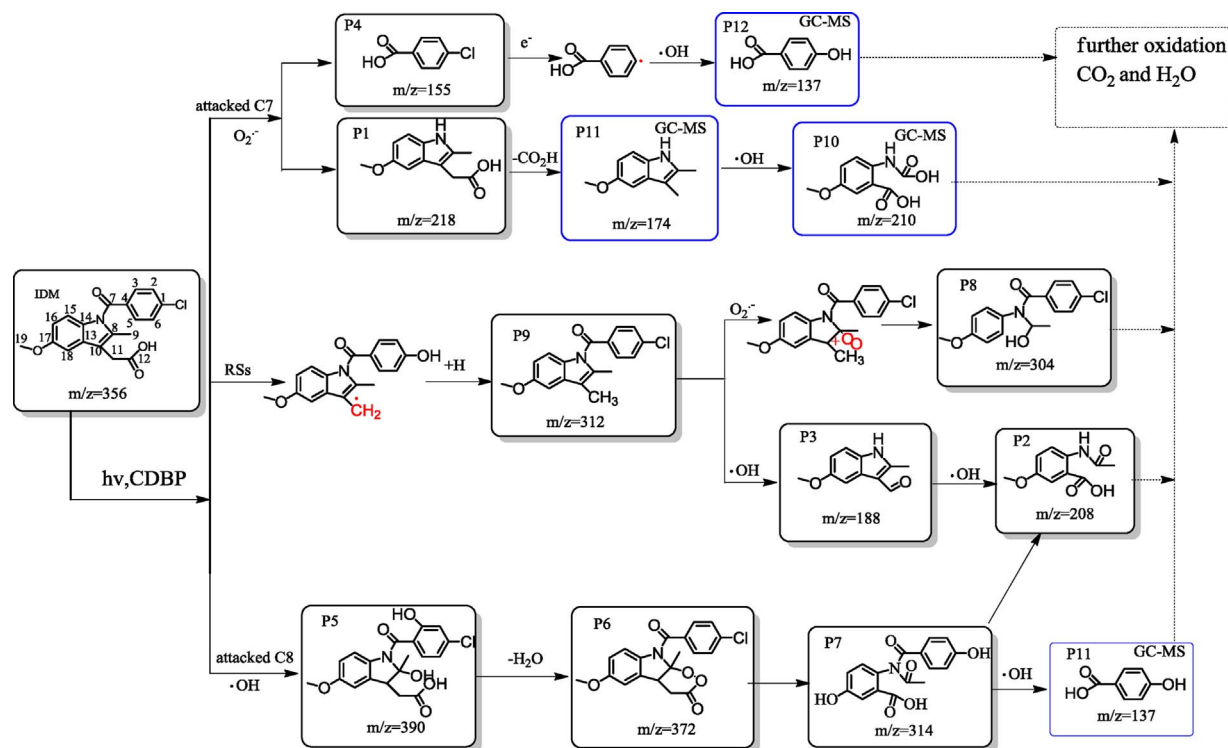


Fig. 6. ESR spectra of the (a)  $\text{DMPO} \cdot \cdot\text{OH}$  and (b)  $\text{DMPO} \cdot \text{O}_2^{\cdot-}$  adducts recorded with pristine  $\text{BiPO}_4$  and 3.0 wt% CDBP under simulated sunlight irradiation, [catalyst] = 1 g/L.



Scheme 1. Possible transformation pathways of IDM in 3.0wt%CDBP aqueous solution under simulated sunlight irradiation.

quenching experiments and ESR analyses.

### 3.5. Photocatalysis mechanism

On the basis of above results and discussion, the potential mechanism for the photocatalytic degradation of IDM by CDBP is proposed and schematically illustrated in Fig. 7. As is well recognized,

wavelengths of less than, or equal to 322 nm, may excite BiPO<sub>4</sub> to produce electron-hole pairs [8]. With the introduction of CDs, a large portion of the visible light was converted to a shorter wavelength due to its up-converted PL properties, which may enhance photocatalytic activity due to an increase in the photogenerated electron-hole pairs.

Fig. 7a shows the photoluminescence of BiPO<sub>4</sub> and 3.0 wt% CDBP, where it may be clearly seen that the fluorescence of CDBP was

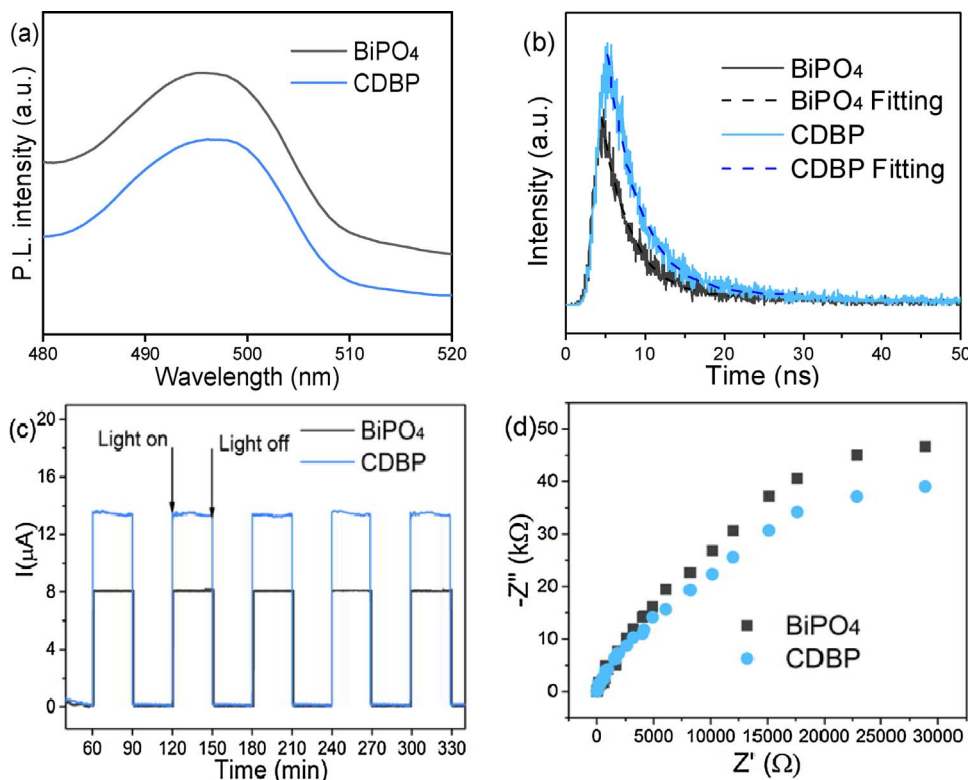


Fig. 7. Photoluminescence spectra (a) and fluorescence decay (b) of BiPO<sub>4</sub> and 3.0 wt% CDBP, excitation at 325 nm; Photocurrent responses (c) and electrochemical impedance spectroscopy (d) of BiPO<sub>4</sub>, 3.0 wt% CDBP and under stimulant sunlight irradiation.



significantly lower than that of the  $\text{BiPO}_4$ , which improved the separation of photo-electron-hole pairs and further enhanced the photocatalytic performance of the CDBP [54]. Moreover, to further understand the charge carrier transfer properties of as-prepared samples, the time-resolved PL spectrum was measured. Fig. 7b is the P.L. delay fitting curves of the  $\text{BiPO}_4$  and CDBP. The lifetime of  $\text{BiPO}_4$  and 3.0 wt% CDBP were 3.7 and 4.1 ns, respectively. This result illustrated the introduction of CDs can efficiently retard the carriers recombination, which were similarly reported by Wu. et al. [22].

Furthermore, the transient photocurrent responses of  $\text{BiPO}_4$  and 3.0 wt% CDBP under light-on and light-off conditions were reversible and stable (Fig. 7c). The photocurrent of 3.0 wt% CDBP was 13  $\mu\text{A}$ , and  $\sim 1.6$  times as high as that of pure  $\text{BiPO}_4$ . The higher photocurrent of the 3.0 wt% CDBP composite photocatalyst indicated that there were close interactions at the  $\text{BiPO}_4$  and CDs interfaces, which illustrated that the CDs can promote the separation of photogenerated electron-hole pairs [5,55]. The interface charge separation efficiency could also be investigated through the electrochemical impedance spectra (EIS) [10]. The smaller the arc radius is, the higher the efficiency of charge transfer is. Fig. 7d showed that the radius of 3.0 wt% CDBP was the smaller the arc radius than  $\text{BiPO}_4$ , implying that the charge transfer efficiency of 3.0 wt% CDBP was the higher. Therefore, it could be concluded that the existence of CDs could accelerate the migration and separation efficiency of photogenerated carriers. Further, Scheme 2 shown, the photogenerated electrons in the CDs might be captured by oxygen, resulting in the generation of  $\text{O}_2^{\cdot-}$  [56,57]. As Mott-Schottky plots shown (Fig. S2), with the known band gap of 3.52 eV for 3.0 wt% CDBP (Fig. 1c), the VB potential of 3.0 wt% CDBP composite can be calculated to be +3.22 eV. As the valence band (VB) position of 3.0 wt% CDBP (+3.22 eV) is more positive than the standard redox potential of  $\cdot\text{OH}/\text{H}_2\text{O}$  (+2.73 eV) and  $\cdot\text{OH}/\text{OH}^-$  (+1.99 eV), the  $h^+$  from  $\text{BiPO}_4$  can oxidize  $\text{OH}^-$  or  $\text{H}_2\text{O}$  to give  $\cdot\text{OH}$  [58]. Meanwhile, from the EPR test, the potent oxidizing properties of the photogenerated  $h^+$ , may also attack the IDM. Generally speaking, the production of ROS, such as  $\cdot\text{OH}$ ,  $h^+$ , and  $\text{O}_2^{\cdot-}$  will attack IDM, leading to its efficient photocatalytic degradation and mineralization.

### 3.6. Toxicity evaluation

Fig. 8 To investigate the potential risks of IDM and its degradation products in water treated by AOPs, the ecotoxicity evolution was evaluated during the CDBP photocatalytic degradation at three different trophic levels, luminescent bacteria *V. fischeri* (15 min), *D. magna* (48 h), and *Chlorella* (96 h). As was shown in Fig. 8, *V. fischeri* (15 min), *D. magna* (48 h), and *Chlorella* (96 h), were inhibited by 43.1%, 50%, and 48.7%, respectively, with a 4 mg/L IDM solution. As is shown on Fig. 8d, at an irradiation time of 60 min, the degradation rate of IDM was  $\sim 67.0\%$ , whereas only  $\sim 21\%$  of the TOC removal rate was achieved. Meanwhile, the three levels of ecotoxicity species exhibited

varying degrees of inhibition at rates of 75%, 75%, and 61%. These results implied that more toxic intermediate products were formed during the CDBP photocatalysis of IDM, with similar results reported by Wang et al. [24]. When IDM was undetectable after 120 min and the removal rate of TOC achieved was  $\sim 38\%$ , the inhibition rate of the treated solution remained at 24%, 12%, and 35% for *V. fischeri* (15 min), *D. magna* (48 h), and *Chlorella* (96 h), respectively. However, under prolonged irradiation, the acute toxicity of the treated solutions decreased due to mineralization. In addition, following 240 min irradiation, the acute toxicity of treated solutions was decreased significantly as was the TOC reduction and dechlorination (byproducts, such as P7, P12). Hence, for safe water treatment an appropriately prolonged irradiation time is recommended in order to reduce ecotoxicities. In summary, these results indicated that CDBP provided a very desirable performance in the reduction of ecotoxicities from IDM.

### 3.7. Cycle test

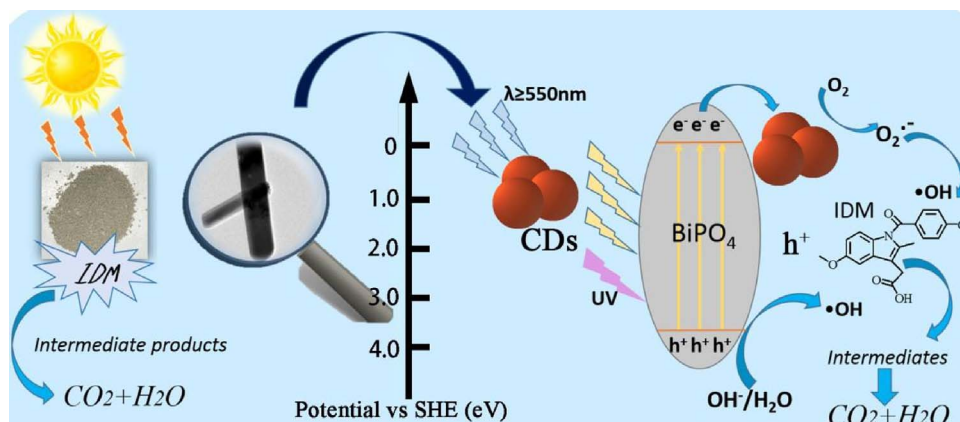
To evaluate the cyclic performance of the CDBP composite, five cycling experiments were carried out for the photodegradation of IDM. As shown in Fig. 9a, after five cycles, there was no obvious decrease in the photocatalytic degradation activity and the XRD pattern remained stable. From the XRD pattern of the CDBP sample (Fig. 9b) it may be seen that there was no obvious change in the crystal morphology. The above results indicated that the CDBP composites showed high stability and reusability under simulated sunlight irradiation.

## 4. Conclusion

A CDs/ $\text{BiPO}_4$  photocatalyst was successfully synthesized via a facile hydrothermal-calcination method. Following the introduction of CDs, the CDs/ $\text{BiPO}_4$  photocatalyst exhibited significantly enhanced activity under simulated sunlight exposure. This demonstrated enhancement might be due to the high separation and easy transfer of photogenerated electron-hole pairs, stronger oxidization attributes, unique up-converted PL properties, as well as band gap narrowing of the CDs. The Ecological Risk Assessment confirmed a decrease in toxicity and TOC reduction with the CDBP complex toward the photodegradation of IDM, which provided an excellent demonstration of photocatalytic CDs composites.

### Acknowledgments

This work was supported by the National Natural Science Foundation of China (No. 21677040 and 21377031), the Innovative Team Program of High Education of Guangdong Province (2015KCXTD007).



**Scheme 2.** Proposed photocatalytic degradation pathways of IDM under simulated sunlight irradiation with 3.0 wt% CDBP composites.

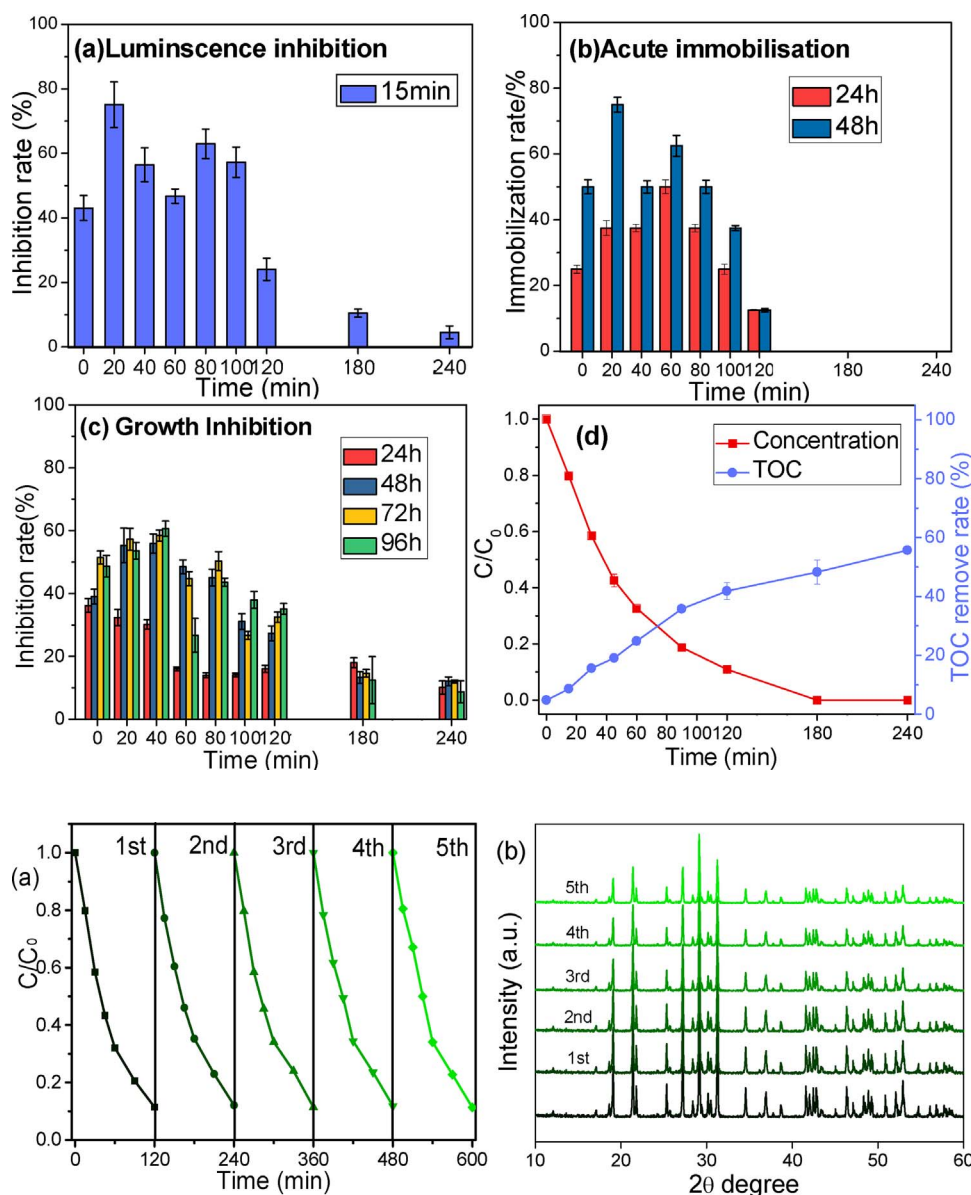


**Fig. 8.** Acute toxicity evaluated with (a) *V. fischeri* for 15 min; (b) *D. magna* for 24 h and 48 h; (c) *Chlorella* for 24 h, 48 h, 72 h and 96 h exposure times; (d) Evolution of both TOC removal efficiencies (blue curve, right y-axis) and IDM degradation rate (red curve, left y-axis) during the photocatalytic degradation of 4 mg/L IDM by 1.0 g/L 3.0 wt% CDBP. (For interpretation of the references to color in this figure legend, the reader is referred to the web version of this article.)

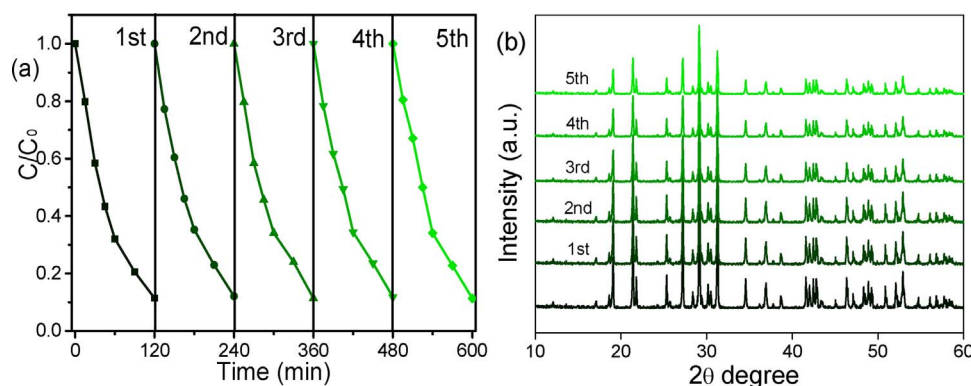


**Fig. 9.** (a) Photocatalytic degradation activity after five cycles of 3.0 wt% CDBP composites under simulated sunlight irradiation; (b) the XRD spectrum of 3.0 wt% CDBP before and 5 cycles photocatalytic experiments.

## Appendix A. Supplementary data

Supplementary data associated with this article can be found, in the online version, at <http://dx.doi.org/10.1016/j.apcatb.2017.09.008>.

## References

- [1] A. Kubacka, M. Fernándezgarcía, G. Colón, *Chem. Rev.* 112 (2016) 1555.
- [2] H. Tong, S. Ouyang, Y. Bi, N. Umezawa, M. Oshikiri, J. Ye, *Adv. Mater.* 24 (2012) 229.
- [3] T. Ji, F. Yang, Y. Lv, J. Zhou, J. Sun, *Mater. Lett.* 63 (2009) 2044–2046.
- [4] A. Hameed, T. Montini, V. Gombac, P. Fornasiero, *J. Am. Chem. Soc.* 130 (2008) 9658.
- [5] Y. Zhu, Y. Wang, Q. Ling, Y. Zhu, *Appl. Catal. B Environ.* 200 (2016) 222–229.
- [6] X. Wu, J. Zhao, S. Guo, L. Wang, W. Shi, H. Huang, Y. Liu, Z. Kang, *Nanoscale* 8 (2016) 17314.
- [7] A. Henríquez, H.D. Mansilla, J. Freire, D. Contreras, *Appl. Catal. B Environ.* 206 (2017) 252–262.
- [8] C. Pan, Y. Zhu, *Environ. Sci. Technol.* 44 (2010) 5570–5574.
- [9] Y. Zhu, L. Qiang, Y. Liu, W. Hua, Y. Zhu, *Appl. Catal. B Environ.* 187 (2016) 204–211.
- [10] Y. Liu, W. Yao, L. Di, R. Zong, Z. Mo, X. Ma, Y. Zhu, *Appl. Catal. B Environ.* 163 (2015) 547–553.
- [11] F. Duo, C. Fan, Y. Wang, Y. Cao, X. Zhang, *Mater. Sci. Semicond. Process.* 38 (2015) 157–164.
- [12] H. Lin, H. Ye, B. Xu, J. Cao, S. Chen, *Catal. Commun.* 37 (2013) 55–59.
- [13] Y. Zhang, B. Shen, H. Huang, Y. He, B. Fei, F. Lv, *Appl. Surf. Sci.* 319 (2014) 272–277.
- [14] C. Pan, J. Xu, Y. Wang, D. Li, Y. Zhu, *Adv. Funct. Mater.* 22 (2012) 1518–1524.
- [15] Y. Zhang, Z.R. Tang, X. Fu, Y.J. Xu, *ACS Nano* 5 (2011) 7426–7435.
- [16] J. Liu, H. Bai, Y. Wang, Z. Liu, X. Zhang, D.D. Sun, *Adv. Funct. Mater.* 20 (2010) 4175–4181.
- [17] X. Liu, L. Pan, T. Lv, G. Zhu, Z. Sun, C. Sun, *Chem. Commun.* 47 (2011) 11984–11986.
- [18] L. Zhang, S. Diao, Y. Nie, K. Yan, N. Liu, B. Dai, Q. Xie, A. Reina, J. Kong, Z. Liu, *J. Am. Chem. Soc.* 133 (2011) 2706–2713.
- [19] C. Zhu, C. Liu, Y. Zhou, Y. Fu, S. Guo, H. Li, S. Zhao, H. Huang, Y. Liu, Z. Kang, *Appl. Catal. B Environ.* 216 (2017) 114–121.
- [20] J. Yu, C. Xu, Z. Tian, Y. Lin, Z. Shi, *New J. Chem.* 40 (2016) 2083–2088.
- [21] Y. Sun, Z. Zhang, A. Xie, C. Xiao, S. Li, F. Huang, Y. Shen, *Nanoscale* 7 (2015) 13974.
- [22] X. Wu, J. Zhao, L. Wang, M. Han, M. Zhang, H. Wang, H. Huang, Y. Liu, Z. Kang, *Appl. Catal. B Environ.* 206 (2017) 501–509.
- [23] P. Chen, F. Wang, Z.F. Chen, Q. Zhang, Y. Su, L. Shen, K. Yao, Y. Liu, Z. Cai, W. Lv, *Appl. Catal. B Environ.* 204 (2017) 250–259.
- [24] F. Wang, P. Chen, Y. Feng, Z. Xie, Y. Liu, Y. Su, Q. Zhang, Y. Wang, K. Yao, W. Lv, *Appl. Catal. B Environ.* 207 (2017) 103–113.
- [25] E.N. Evgenidou, I.K. Konstantinou, D.A. Lambropoulou, *Sci. Total Environ.* 505 (2015) 905–926.
- [26] T. Qiao, Z. Yu, X. Zhang, D.W. Au, *J. Environ. Monit. Jem* 13 (2011) 3097–3103.
- [27] P. Chen, F.L. Wang, K. Yao, J.S. Ma, F.H. Li, W.Y. Lv, G.G. Liu, *Bull. Environ. Contam. Toxicol.* 96 (2016) 203–209.
- [28] C.I. Kosma, D.A. Lambropoulou, T.A. Albanis, *Sci. Total Environ.* 467 (2014) 421–438.

- [29] J. Huang, Y. Wang, G. Liu, C. Ping, F. Wang, J. Ma, F. Li, H. Liu, W. Lv, *Environ. Sci. Pollut. Res. Int.* (2017) 1–10.
- [30] S. Basha, D. Keane, A. Morrissey, K. Nolan, M. Oelgemöller, J. Tobin, *Ind. Eng. Chem. Res.* 49 (2010) 584–595.
- [31] S. Qu, X. Wang, Q. Lu, X. Liu, L. Wang, *Angew. Chem. (International ed. in English)* 51 (2012) 12215.
- [32] Y.Y. Zhu, Y.F. Liu, Y.H. Lü, H. Wang, Q. Ling, Y.F. Zhu, *Acta Phys. Chim. Sin.* 29 (2013) 576–584.
- [33] G. Li, N. Xin, Y. Gao, T. An, *Appl. Catal. B Environ.* 180 (2016) 726–732.
- [34] X. Zhu, Y. Chang, Y. Chen, *Chemosphere* 78 (2010) 209–215.
- [35] J. Zhang, Y. Ma, Y. Du, H. Jiang, D. Zhou, S. Dong, *Appl. Catal. B Environ.* 209 (2017) 253–264.
- [36] H. Wang, P. Sun, S. Cong, J. Wu, L. Gao, Y. Wang, X. Dai, Q. Yi, G. Zou, *Nanoscale Res. Lett.* 11 (2016) 27.
- [37] J. Zhang, X. Zhang, S. Dong, X. Zhou, S. Dong, J. Photochem. Photobiol. A Chem. 325 (2016) 104–110.
- [38] H. Zhang, H. Huang, H. Ming, H. Li, L. Zhang, Y. Liu, Z. Kang, *J. Mater. Chem.* 22 (2012) 10501–10506.
- [39] Y. Liu, Y. Lv, Y. Zhu, D. Liu, R. Zong, Y. Zhu, *Appl. Catal. B Environ.* 147 (2014) 851–857.
- [40] Y. Hu, J. Yang, J. Tian, L. Jia, J.S. Yu, *Carbon* 77 (2014) 775–782.
- [41] C. Pan, J. Xu, Y. Chen, Y. Zhu, *Appl. Catal. B Environ.* 115–116 (2012) 314–319.
- [42] J. Yu, N. Song, Y.K. Zhang, S.X. Zhong, A.J. Wang, J. Chen, *Sensors Actuat. B Chem.* 214 (2015) 29–35.
- [43] L. Wang, F. Ruan, T. Lv, Y. Liu, D. Deng, S. Zhao, H. Wang, S. Xu, *J. Lumin.* 158 (2015) 1–5.
- [44] C. Pan, J. Xu, Y. Wang, D. Li, Y. Zhu, *Adv. Funct. Mater.* 22 (2012) 1518–1524.
- [45] J. Pan, Y. Sheng, J. Zhang, J. Wei, P. Huang, X. Zhang, B. Feng, *J. Mater. Chem. A* 2 (2014) 18082–18086.
- [46] X. Zhang, M. Feng, L. Wang, R. Qu, Z. Wang, *Chem. Eng. J.* 307 (2017) 95–104.
- [47] Y. Wang, S. Indrawirawan, X. Duan, H. Sun, H.M. Ang, M.O. Tade, S. Wang, *Chem. Eng. J.* 266 (2015) 12–20.
- [48] H. Wang, Y. Su, H. Zhao, H. Yu, S. Chen, Y. Zhang, X. Quan, *Environ. Sci. Technol.* 48 (2014) 11984–11990.
- [49] C. Sousa, S. Tosoni, F. Illas, *Chem. Rev.* 113 (2013) 4456–4495.
- [50] L. Novakova, L. Matysova, L. Havlikova, P. Solich, *J. Pharm. Biomed. Anal.* 37 (2005) 899–905.
- [51] P. Chen, F. Wang, Q. Zhang, Y. Su, L. Shen, K. Yao, Z.-F. Chen, Y. Liu, Z. Cai, W. Lv, G. Liu, *Chemosphere* 172 (2017) 193–200.
- [52] K. Pitchumani, D. Madhavan, *Cheminform* 35 (2004).
- [53] F. Temussi, F. Cermola, M. Dellagrecia, M.R. Iesce, M. Passananti, L. Previtera, A. Zarrelli, *J. Pharm. Biomed. Anal.* 56 (2011) 678.
- [54] X. Pu, D. Zhang, Y. Gao, X. Shao, G. Ding, S. Li, S. Zhao, *J. Alloys Compd.* 551 (2013) 382–388.
- [55] X. Yu, J. Liu, Y. Yu, S. Zuo, B. Li, *Carbon* 68 (2014) 718–724.
- [56] J. Ma, C. Wang, H. He, *Appl. Catal. B Environ.* 184 (2016) 28–34.
- [57] G. Li, N. Xin, J. Chen, J. Qi, T. An, P.K. Wong, H. Zhang, H. Zhao, H. Yamashita, *Water Res.* 86 (2015) 17.
- [58] D. Wu, B. Wang, W. Wang, T. An, G. Li, T.W. Ng, H.Y. Yip, C. Xiong, H.K. Lee, P.K. Wong, *J. Mater. Chem. A* 3 (2015) 15148–15155.